

IMAGING THE HELIOSPHERE USING NEUTRAL ATOMS FROM SOLAR WIND ENERGY DOWN TO 15 eV

A. GALLI¹, P. WURZ¹, S. A. FUSELIER^{2,3}, D. J. MCCOMAS^{2,3}, M. BZOWSKI⁴,
J. M. SOKÓŁ⁴, M. A. KUBIAK⁴, AND E. MÖBIUS⁵

¹ Physics Institute, University of Bern, Bern 3012, Switzerland

² Southwest Research Institute, San Antonio, TX 78228, USA

³ University of Texas, San Antonio, TX 78249, USA

⁴ Space Research Centre, Polish Academy of Sciences, Warsaw 00-716, Poland

⁵ University of New Hampshire, Durham, NH 03824, USA

Received 2014 July 10; accepted 2014 September 20; published 2014 October 29

ABSTRACT

We study the spatial and temporal distribution of hydrogen energetic neutral atoms (ENAs) from the heliosheath observed with the IBEX-Lo sensor of the *Interstellar Boundary Explorer* (IBEX) from solar wind energies down to the lowest available energy (15 eV). All available IBEX-Lo data from 2009 January until 2013 June were included. The sky regions imaged when the spacecraft was outside of Earth’s magnetosphere and when the Earth was moving toward the direction of observation offer a sufficient signal-to-noise ratio even at very low energies. We find that the ENA ribbon—a 20° wide region of high ENA intensities—is most prominent at solar wind energies whereas it fades at lower energies. The maximum emission in the ribbon is located near the poles for 2 keV and closer to the ecliptic plane for energies below 1 keV. This shift is an evidence that the ENA ribbon originates from the solar wind. Below 0.1 keV, the ribbon can no longer be identified against the globally distributed ENA signal. The ENA measurements in the downwind direction are affected by magnetospheric contamination below 0.5 keV, but a region of very low ENA intensities can be identified from 0.1 keV to 2 keV. The energy spectra of heliospheric ENAs follow a uniform power law down to 0.1 keV. Below this energy, they seem to become flatter, which is consistent with predictions. Due to the subtraction of local background, the ENA intensities measured with IBEX agree with the upper limit derived from Ly α observations.

Key words: ISM: general – plasmas – solar wind – Sun: heliosphere

Online-only material: color figures

1. INTRODUCTION

The *Interstellar Boundary Explorer* (IBEX) has been observing the interaction of the heliosphere with the surrounding interstellar medium since 2009 January (McComas et al. 2009a). The scientific payload consists of two sensors, IBEX-Lo (Fuselier et al. 2009) and IBEX-Hi (Funsten et al. 2009). IBEX-Lo measures energetic neutral atoms (ENAs) in eight energy steps from 0.01 to 2 keV, IBEX-Hi is sensitive to ENAs between 0.3 and 6 keV energy. The two sensors are based on different ENA detection techniques (a conversion surface in the case of IBEX-Lo, a thin foil in the case of IBEX-Hi), which allows for an instrument-independent confirmation of the heliospheric ENA signals at overlapping energies. The two cameras are pointed almost perpendicularly toward the Sun direction with an instantaneous field of view (FOV) of roughly 6:5 \times 6:5 while the spacecraft spins around an axis pointing toward the Sun. As IBEX follows Earth on its orbit around the Sun, every pixel of the sky is imaged at least twice a year in every energy step.

Hydrogen ENAs are the result of charge exchange between a fast proton and a neutral atom. For heliospheric ENAs, the protons originate from the solar wind or from pick-up ions. The neutral atoms for charge exchange originate from the local interstellar matter (LISM) that surrounds the heliosphere. The ENAs visible in the IBEX sensors are expected to be produced in the shocked solar wind in the inner heliosheath, i.e., the region between the termination shock and the heliopause (Fuselier et al. 2014). The termination shock at a heliocentric distance between 80 and 100 AU (Burlaga et al. 2008; Richardson et al.

2008) marks the boundary between supersonic and subsonic solar wind, the heliopause separates the solar wind plasma from the outer heliosheath dominated by the LISM.

The first years of IBEX observations (McComas et al. 2009b) revealed a spatial distribution of heliospheric ENAs that was completely unexpected from earlier predictions (e.g., Gruntman et al. (2001)). At solar wind energies, a 20° wide “ribbon” of high ENA intensities winds around an ENA “hole” of very low intensities. The latter is offset from the downwind direction (at 79° ecliptic longitude) by at least 40° (McComas et al. 2013). The existence of the ENA ribbon seems to indicate additional ENA production processes. One possibility would be neutralized solar wind that leaves the heliosphere to be reionized and neutralized again in the outer heliosheath (for a recent review on possible explanations for the ribbon see McComas et al. (2014b)).

For general review papers on heliospheric ENAs observed with IBEX (with a focus on IBEX-Hi observations), the reader may refer to McComas et al. (2012) and McComas et al. (2014a). The present study of low energy ENAs builds on the two previous publications on IBEX-Lo observations by Fuselier et al. (2012) and Fuselier et al. (2014). We now quantify and carefully subtract the background and we suppress the strong signal produced by the LISM inflow. This allows us to create the first heliospheric ENA maps at the lowest energies in IBEX-Lo. The maps reveal the ENA ribbon and other structures at energies much lower than solar wind energies (typical energy \approx 1 keV), and they help us define regions of high signal-to-noise ratio. This allows us to test if the energy spectrum of heliospheric ENAs

starts to roll over at low energies as expected from theory and inferred from Ly α observations of neutral hydrogen in the LISM (Wood et al. 2007). Previously, Fuselier et al. (2014) concluded from the disagreement between Ly α observations and IBEX-Lo intensities below 0.1 keV that the latter must be interpreted as an upper limit of the true signal.

In Section 2, we present the data set, the method of reconstructing ENA intensities with the corresponding uncertainties from raw data and how we correct for background sources. Section 3 summarizes the results with three subsections on ENA intensity maps, energy spectra, and the temporal evolution of the ENA signal from 2009 to 2013. Section 4 concludes the paper.

2. METHOD

In this section, we explain how we derived ENA intensity maps and energy spectra from raw count rates measured with IBEX-Lo. Section 2.1 gives details on the observation times, Section 2.2 lists the steps necessary to convert raw count rates into corrected ENA intensities, in Section 2.3 we present the three most important background sources, and Section 2.4 wraps up this chapter with the error analysis for ENA intensity maps and energy spectra.

We developed an experimental mapping algorithm that is similar to the approach used for the data products presented by McComas et al. (2014a). The differences between the two approaches are explained in detail in the Appendix at the end of the paper. The differences were dictated by the scope of this study, namely the very low energies of heliospheric ENAs. The encountered background sources could only be quantified with a full Compton–Getting transformation of the intensity maps. The background subtraction and various transformation steps also called for a thorough reanalysis of the absolute uncertainties. The ENA intensity maps derived with the approach for this study agree with the IBEX-Lo maps for energy steps 5–8 in Figure 14 of McComas et al. (2014a) within the uncertainties for the all-sky direction in the spacecraft frame. The insights gained from the experimental mapping algorithm will be exploited for future data product releases.

2.1. Observations

The data set for this study covers the first years of *IBEX* observations from orbit 14 (2009 January) to orbit 209b (2013 June). The observation time was divided into five winter (November until April) and five summer (May and June) seasons. We discarded the observations from July to October when *IBEX* was inside the magnetosphere because local backgrounds are high during that period (Fuselier et al. 2014). This left us with the portion of the *IBEX* orbit highlighted in green in Figure 1. The list of good IBEX-Lo observation times also excludes any time interval when the FOV points to the magnetosphere or to the Moon.

The distinction between ram and antiram observations is important for the whole analysis because *IBEX* moves on its Earth orbit at a speed of roughly 30 km s⁻¹ relative to the heliosphere. During a ram observation, *IBEX* is moving toward the observed region in the sky. An example in Figure 1 is the LISM inflow observed in February. Half a year later, *IBEX* images the same direction again while moving away from it. The raw ENA intensity measured from the same direction in the sky becomes notably higher for ram than for antiram observations when the relative motion of the spacecraft exceeds about 10% of the ENA velocity. For hydrogen ENAs, this condition applies

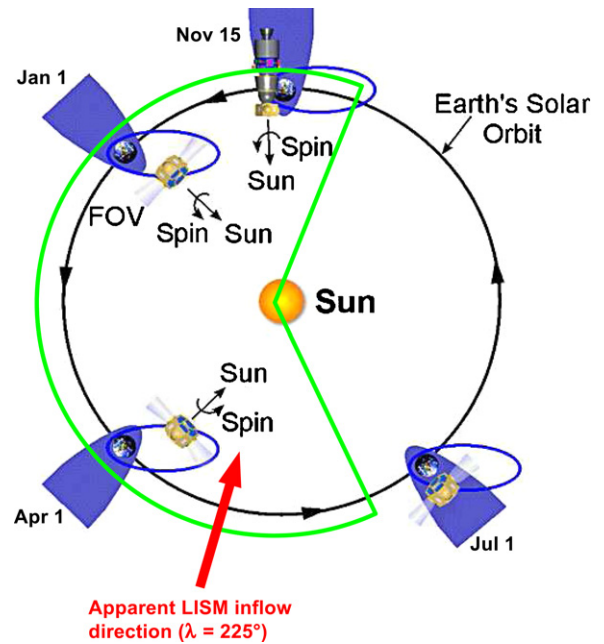


Figure 1. Configuration of IBEX-Lo observations: the green region denotes the time span from November to June when *IBEX* is outside the terrestrial magnetosphere (blue cones) for most of the orbits, the remaining 4.5 months are difficult observation times for low energy ENAs. The red arrow indicates apparent inflow direction of helium from LISM, which is seen most prominently in the first week of February.

(A color version of this figure is available in the online journal.)

to energies below 0.4 keV. ENA maps that include only ram observations are cleaner because higher raw ENA intensities imply a better signal-to-noise ratio in the presence of a local background. Unfortunately, the length of the “magnetospheric season” from July to October means that ram-only maps will cover just 220° (from 140° to 360° ecliptic longitude) out of the 360° full sky.

2.2. Generation of ENA Intensity Maps in the Solar Inertial Frame

We assembled full-sky maps of count rates for each of the 10 observation seasons in ecliptic coordinates. The maps were organized in pixels of 6° × 6° in a cylindrical projection to reflect the intrinsic *IBEX* FOV. We corrected the raw count rates for the data throughput effect and the sputtering from higher energies, we excluded pixels affected by LISM inflow (see Section 2.3), and we subtracted the local background count rate (see Section 2.3). The remaining count rates were assumed to originate from true heliospheric hydrogen ENAs. The count rates c were converted into raw differential intensities (j_m , in units of cm⁻² sr⁻¹ s⁻¹ keV⁻¹) by

$$j_m = \frac{c}{G_0 \varepsilon(E)} \frac{E}{\Delta E} \frac{1}{E}, \quad (1)$$

using the same geometric factor G_0 , energy-dependent efficiencies $\varepsilon(E)$, and the width of energy steps $\Delta E/E = 0.7$ as in previous *IBEX*-Lo publications. Equation (1) was applied to each of the eight energy bins of *IBEX*-Lo, their central energies E are 0.015 keV (bin 1), 0.029 keV (bin 2), 0.055 keV (bin 3), 0.11 keV (bin 4), 0.209 keV (bin 5), 0.439 keV (bin 6), 0.872 keV (bin 7), and 1.821 keV (bin 8). The raw intensities from Equation (1) were then corrected for reionization losses inside the termination shock and for the Compton–Getting effect

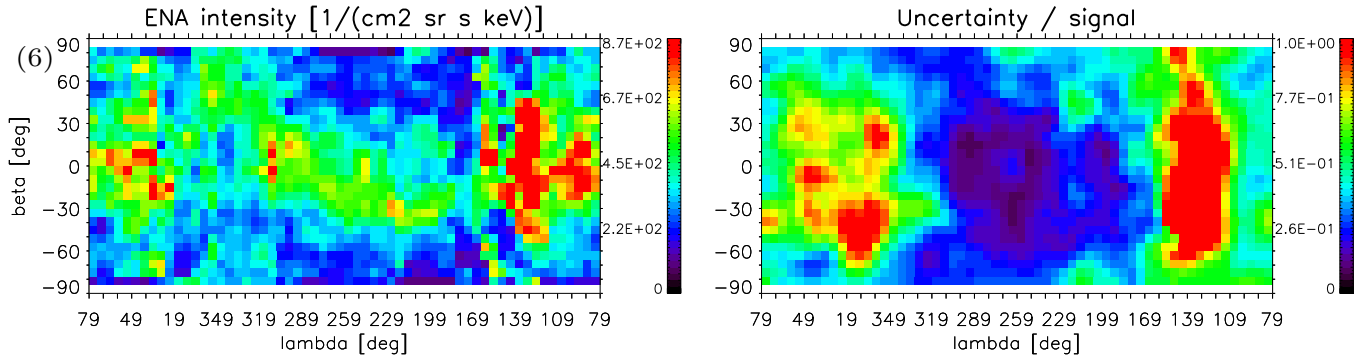


Figure 2. Magnetospheric contamination illustrated for energy bin 6 of IBEX-Lo, spanning five years of observations. The left panel shows average corrected ENA intensity in units of $\text{cm}^{-2} \text{sr}^{-1} \text{s}^{-1} \text{keV}^{-1}$, the right panel shows the relative uncertainty introduced by magnetospheric contamination.

(A color version of this figure is available in the online journal.)

to obtain the ENA intensities in the inertial reference frame of the heliosphere. This procedure yielded sky maps of corrected ENA intensities for the 10 different seasons for each of the eight IBEX-Lo energy steps. With the exception of Section 3.3, only the ENA intensity maps averaged over all 10 seasons will be discussed. Six months would be sufficient for a complete map coverage, but several years of data were required for acceptable statistics (see Section 2.4).

The Compton–Getting correction is mandatory if we want to interpret the observations below 0.4 keV because the corrected ENA intensity differs from the raw intensity by more than a factor of two at these energies. Our algorithm follows the same principles as employed by McComas et al. (2012) for IBEX-Hi and by Galli et al. (2013). We transformed the measured ENA intensities into the solar inertial reference frame at the center energy of the eight IBEX-Lo energy steps. For a given map pixel and energy, we considered the maps of this energy and of the next higher energy step. We selected the four pixels adjacent to the direction (λ_m, β_m) that is shifted to the current pixel by the Compton–Getting correction. This approach smoothed spatial patterns smaller than $12^\circ \times 12^\circ$ in the corrected ENA maps, but the alternative would have been small-scale artifacts. We then corrected the measured intensities of the four pixels for the survival probability of a hydrogen ENA for the given direction and time (Bzowski et al. 2013; Sokół et al. 2013; McComas et al. 2012), and we fit a power law with spectral slope γ through the data points. We fit the spectral slope individually for each map pixel and for each pair of energy bins, the only constraint being $-5 \leq \gamma \leq +1$. Finally, we transformed the intensity from the moving reference frame j_m to the solar reference frame by

$$j = j_m \left(1 + \frac{u^2}{v^2} + \cos \beta_m \frac{u_x \cos \lambda_m + u_y \sin \lambda_m}{v} \right)^{-\gamma-1}. \quad (2)$$

The velocity vector of the spacecraft with respect to the ecliptic reference frame is $\mathbf{u} = (u_x, u_y, u_z)$, and $v = \sqrt{2E/m}$ is the ENA velocity that corresponds to the energy E at which j_m was measured. Spacecraft motion out of the ecliptic plane was neglected, i.e., $u_z = 0$ in Equation (2). The final j is the average over the four neighboring pixels. It will be referred to as corrected ENA intensity throughout this paper.

2.3. Background Sources

For several reasons, observations at low ENA energies (energy steps 1–5 of IBEX-Lo) are more affected by nonheliospheric signals than observations at solar wind energies. First,

the detection efficiency decreases with energy, resulting in poorer statistics. Second, local background sources become more important in absolute count rates at low energies. Third, the correction for Compton–Getting and survival probability (Section 2.2) makes the result very vulnerable to any unidentified local background that should have been removed before transforming the signal from the spacecraft frame into the inertial reference frame. This problem is more pronounced for antiram observations because the ratio of true signal to background signal is much lower.

During analysis, we identified three different background sources that must be excluded before reconstructing the true heliospheric signal: contamination from the Earth’s magnetosphere, sputtered hydrogen from helium and heavy neutrals of the LISM, and a ubiquitous local background source. We will now discuss these background sources and explain how we separated them from the heliospheric signal.

Because the magnetospheric contamination is highly variable with time and energy, we assessed its effect empirically. We created an alternative data set of IBEX-Lo observation times limited to ± 24 hours around *IBEX* apogee for each orbit. The pixel-by-pixel standard deviation over all 10 seasons between the two different data sets was interpreted as the uncertainty introduced by magnetospheric contamination. The rationale for this approach is that the heliospheric signal should not depend on the distance between *IBEX* and the Earth. This yielded a map of magnetospheric contamination for all eight energy steps. Figure 2 presents the result for energy step 6 (0.439 keV): the left panel shows corrected intensities in $\text{cm}^{-2} \text{sr}^{-1} \text{s}^{-1} \text{keV}^{-1}$ averaged over five years, the right panel shows the relative uncertainty of the signal due to magnetospheric contamination. All maps in this paper show ecliptic coordinates λ (longitude) and β (latitude) centered on $(\lambda = 259^\circ, \beta = 0^\circ)$. The longitude corresponds to the nose of the heliosphere or upwind direction of the LISM (Bzowski et al. 2012; Möbius et al. 2012), the left and right boundary at $\lambda = 79^\circ$ correspond to downwind direction. Unfortunately, the statistics proved insufficient to quantify the magnetospheric contamination for a single season or to subtract the magnetospheric background from the heliospheric signal. The apogee data set was therefore used only to estimate the impact of magnetospheric contamination, for all other purposes, we relied on the longer observation times. In all energies, the ecliptic longitudes between 130° and 170° are most heavily affected (red stripes in Figure 2) by the magnetosphere. This also holds true for IBEX-Hi observations at higher energies (McComas et al. 2012), but at lower energies the contamination becomes

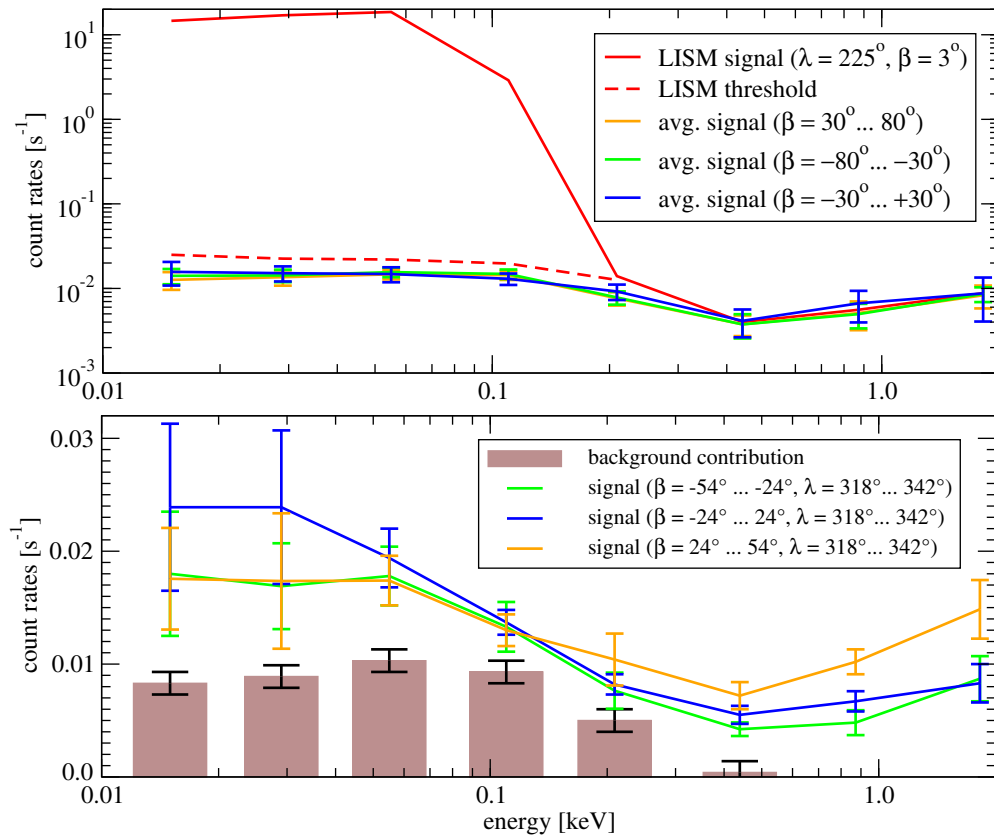


Figure 3. Spectra of uncorrected count rates, averaged over all five years of ram maps outside the LISM inflow (orange, blue, and green lines in both panels). The spectrum at the center of the LISM inflow direction has been added as a red line in the upper panel (note the logarithmic y axis). The dashed red line indicates the average uncontaminated signal plus its 3σ variability. Any pixel with a count rate above this threshold is considered to be contaminated by LISM. The contribution of the ubiquitous background to the signal is depicted by gray bars in the lower panel on a linear y axis.

(A color version of this figure is available in the online journal.)

more notable, both in terms of intensity and angular spread. The right panel in Figure 2 indicates that the intensities around the nominal downwind direction (left map boundary, $\lambda = 79^\circ$) are also affected. As will be shown in Section 3, the magnetospheric background basically restricted clean heliospheric maps at low energies to observations in the ram direction.

The study of neutral interstellar atoms is one of the main scientific goals of IBEX-Lo, and the sensor performs very well for this task. IBEX-Lo provided the scientific community with a series of new results about the direction and velocity (Bzowski et al. 2012; Möbius et al. 2012; Schwadron et al. 2013), chemical composition (e.g., Bochsler et al. 2012; Saul et al. 2013), and D/H isotope ratio of the LISM (Rodriguez et al. 2013, 2014). For the present study, the inflowing LISM is a background that dominates the weak ENA signal from the heliosphere. The upper panel of Figure 3 shows energy spectra of averaged count rates for the eight IBEX-Lo channels. The red curve belongs to the center of the LISM inflow, the three other curves (blue, orange, and green) were chosen from regions that are not affected by the LISM signal. The apparent direction of the LISM inflow ($\lambda = 225^\circ$) is not identical with the true LISM upwind direction ($\lambda = 259^\circ$) because the interstellar atoms are deflected from their trajectory as they approach the Sun (Möbius et al. 2012). Proceeding from high to lower energies of IBEX-Lo, the LISM signal appears around 0.2 keV. Here it is produced mainly by neutral oxygen and neon atoms that sputter hydrogen atoms from the conversion surface of the instrument. In the lower four energy bins, the LISM signal reaches count

rates three orders of magnitude higher (note the logarithmic scale in the upper panel of Figure 3) than the heliospheric ENA signal. These count rates originate mainly from neutral LISM helium sputtering hydrogen atoms. In the two lowest energy bins neutral LISM hydrogen adds to the signal (Saul et al. 2013; Rodriguez et al. 2013). In parallel to this study, McComas et al. (2014a) developed a technique to remove the signal caused by sputtering from LISM neutrals in energy steps 5 and 6. At the four lowest energy bins, the strength and spatial extent of the LISM signal make it impossible to subtract it from the heliospheric signal without making strong assumptions about the LISM signal and the underlying heliospheric signal. Kubiak et al. (2014) showed that the LISM signal seen in energy step 2 can be modeled in most cases as sputtering from pristine neutral interstellar helium plus a weaker and more extended spot produced by warmer and slower neutral helium dubbed the “Warm Breeze.” We experimented with subtracting these signals from the surrounding heliospheric signal but decided against it for this study. The process generating the Warm Breeze is not fully understood. The choice of any fit function far away from the LISM peak therefore cannot be motivated theoretically, which would imply arbitrary results for the derived heliospheric signal. Moreover, even the Warm Breeze component is usually an order of magnitude more intense than the heliospheric signal (Kubiak et al. 2014). To use as few assumptions as possible, we therefore blanked out the pixels affected by the LISM inflow and only examined the reconstructed heliospheric ENA intensities of the remaining regions. The threshold between a clean and

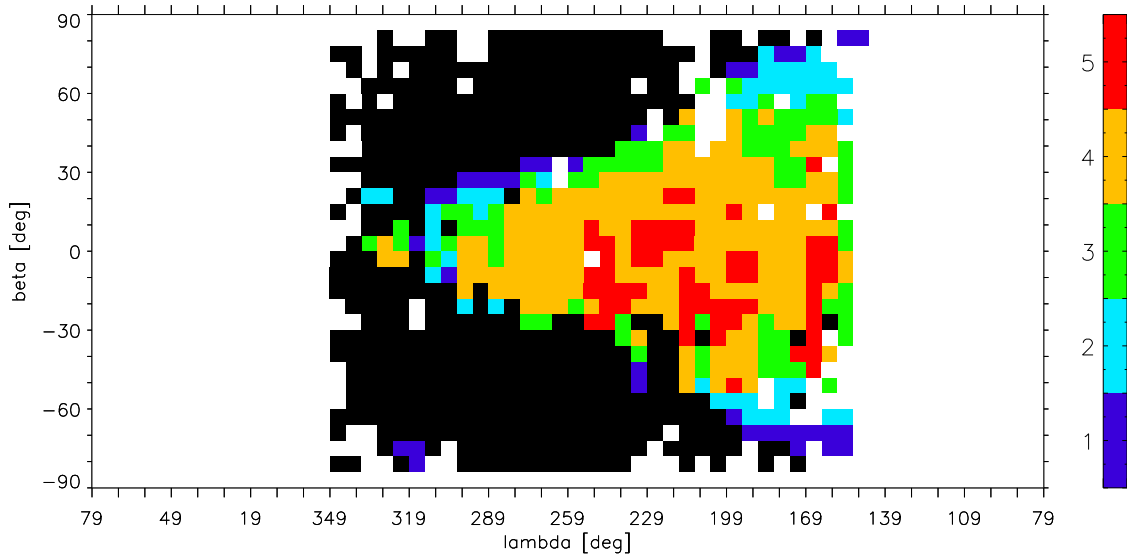


Figure 4. Ram map indicating the extent of the LISM inflow contamination. Red: ENA intensity higher than LISM threshold in all five energy steps from 1 to 5; dark blue: ENA intensity exceeds LISM threshold only in the lowest energy bin. The lower the energy of measured ENAs, the broader the spatial distribution of LISM inflow. Regions of black pixels yield the best estimate for energy spectra because there is no recognizable LISM contamination.

(A color version of this figure is available in the online journal.)

an LISM-contaminated spectrum was assumed to be the mean plus three standard deviations of all raw count rates from ram observations outside the LISM inflow region. The same criterion was used for all five energy steps affected by LISM sputtering. The threshold values are illustrated by a red dashed curve in energy steps 1–5 in the upper panel of Figure 3. Figure 4 shows the pixels of the averaged count rates in ram direction that are contaminated by the LISM signal according to the definition from Figure 3. The color code from 1 to 5 relates to the five lower energy bins, i.e., (1) only energy bin 1 is contaminated, (5) all energy bins from 1 to 5 are contaminated. The orange pixels are due to neutral helium, the wedge of pixels that are contaminated only in energy step 1 or 2 was caused by neutral hydrogen (Saul et al. 2013; Rodriguez et al. 2013). The region of LISM contamination expands in the maps of lower energies because the trajectories of low-energetic LISM atoms exhibit a larger scatter and because hydrogen LISM adds to the signal. As a consequence, the regions available for heliospheric ENA observations shrink as we proceed to lower energies.

The magnetospheric background and the LISM signal pose a problem to the evaluation of heliospheric ENAs, but the origins of the signals are well understood. The third background source must be local, but its nature is unclear. It depends on energy but is invariant to observation direction, year, and distance to Earth. The latter is concluded from the fact that the background levels for the nominal and for the apogee data set are identical although the average distance of *IBEX* to Earth changes. Because of this invariance to the observation time and direction, we consider an instrument-related cause to be most likely. The principle to identify this ubiquitous background was put forth by Fuselier et al. (2014). We compared the corrected intensities for the ram and antiram observations of viewing directions that are not affected by magnetospheric contamination or LISM inflow. For this purpose, we chose the sector between 300° and 360° ecliptic longitude and assumed that the heliospheric signal should be constant over the six months separating the ram from the antiram observations. For the selected regions, the raw intensity was significantly higher for ram than for antiram direction. However, when we interpreted the whole signal as heliospheric ENAs

Table 1
Background Count Rates in the Lower Energies of
IBEX-Lo Derived from All Five Years of Data

Energy	Background Count Rate in s^{-1}
0.015 keV	0.0083 ± 0.001
0.029 keV	0.0089 ± 0.001
0.055 keV	0.0103 ± 0.001
0.110 keV	0.0093 ± 0.001
0.209 keV	0.0050 ± 0.001
0.439 keV	0.0004 ± 0.001
0.872 keV	0.0
1.821 keV	0.0

Note. The background was quantified by demanding that the heliospheric ENA signal in the solar inertial reference frame (between 300° and 360° ecliptic longitude) should be equal for ram and antiram observations after background subtraction.

and corrected the raw intensities according to Section 2.2, the resulting intensities were always higher for the antiram direction. The correction algorithm thus over-compensated for the proper motion of the spacecraft. We resolved this discrepancy by postulating a local background source that must be subtracted before the signal can be transformed from the spacecraft to the inertial reference frame. With $F()$ denoting the transformation to the inertial frame, we fit a local background b_k for energy bins $k = 1-6$ to obtain the transformed heliospheric ENA intensities that are identical for ram and antiram directions:

$$F(j_{k, \text{ram}} - b_k) = F(j_{k, \text{antiram}} - b_k), \quad k = 1, \dots, 6. \quad (3)$$

We repeated this fit procedure for three regions in the southern and northern hemisphere and in the ecliptic plane; the retrieved parameters b differed by only $\sim 10\%$ among the different regions. This variability was used as the uncertainty of b . The background parameters did not change when we considered different years of the data set. The parameters with their uncertainty are listed in Table 1 and are plotted as gray bars in the lower panel of Figure 3.

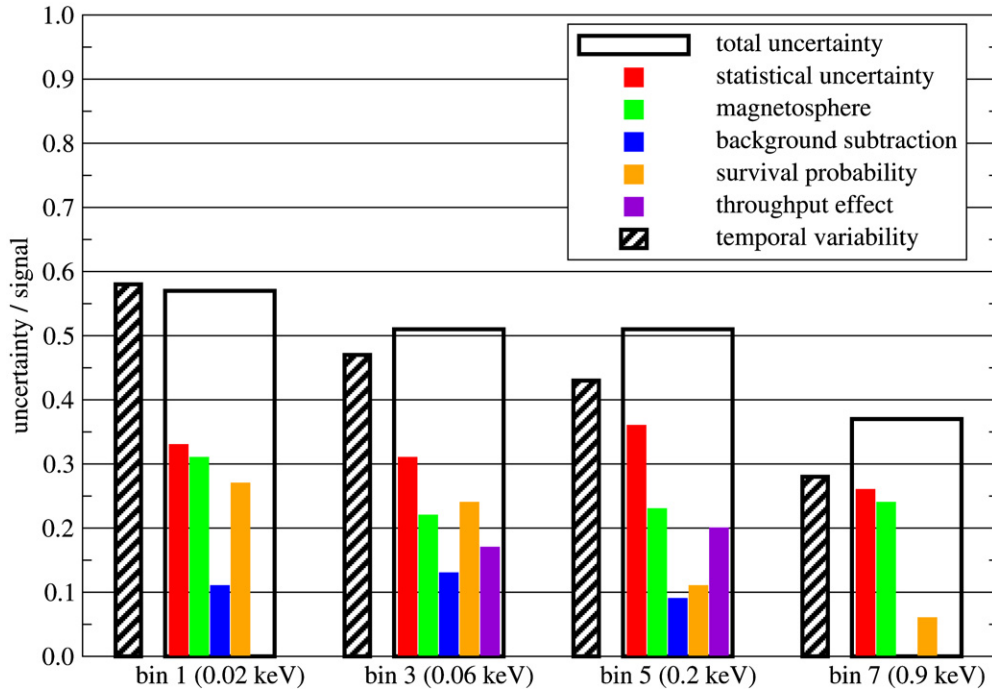


Figure 5. Relative uncertainty of a single map pixel of reconstructed ENA intensities for a five-year average for ram observations. The total uncertainty from error analysis is shown by the black bars that include the five different error sources (red: statistical uncertainty, green: magnetospheric contamination, blue: uncertainty of subtracted background, orange: uncertainty of survival probability, purple: uncertainty of dead time effect). The striped bars represent the observed temporal variability of the signal over five years.

(A color version of this figure is available in the online journal.)

They do not differ significantly from zero above 0.2 keV, whereas they contribute roughly half of the total count rates at energies below 0.2 keV. After having established the background levels, we subtracted them from all measurements. The result was considered the best estimate of the true heliospheric ENA signal arriving at *IBEX* at 1 AU heliocentric distance and was transformed to corrected ENA intensities as described in Section 2.2.

2.4. Uncertainties

At lower energies, a thorough error analysis becomes indispensable because the sum of statistical and systematic error sources exceeds the heliospheric signal for some observation directions. We estimated the total uncertainty σ_j for each pixel and energy of corrected ENA intensities j separately as a square sum of four independent error sources (magnetospheric contamination, uncertainty of reionization losses, uncertainty of background subtraction, and the purely statistical error of count rates) times the uncertainty of the data throughput ratio:

$$\sigma_j = \sigma_{\text{th}} \sqrt{\sigma_{\text{stat}}^2 + (j_{\sigma, \text{magn}} - j)^2 + (j_{\sigma, \text{back}} - j)^2 + (j_{\sigma, \text{sp}} - j)^2}. \quad (4)$$

The statistical error was derived from Poisson statistics of the absolute counts in the pixel C summed over all 10 seasons,

$$\frac{\sigma_{\text{stat}}}{j} = \frac{\sqrt{\sum_{i=1}^{10} C_i}}{\sum_{i=1}^{10} C_i}, \quad (5)$$

and the error contribution from the data throughput correction was estimated to $\sigma_{\text{th}} = 1.0, 1.0, 1.06, 1.20, 1.09, 1.0, 1.0,$ and 1.0 for energy steps 1–8. The error contributions from

magnetospheric contamination, background subtraction, and uncertainty of survival probability were estimated from average maps of corrected ENA intensity ($j_{\sigma, \text{magn}}, j_{\sigma, \text{back}}, j_{\sigma, \text{sp}}$) for which we varied the parameter in question by 1σ from its default value. The uncertainties of the background levels and of the survival probabilities did not depend on time or viewing direction. For the survival probability, relative uncertainties of 50%, 35%, 25%, 20%, 15%, 10%, 5%, and 5% were assumed for energy steps 1–8, the uncertainties of the background are listed in Table 1. For magnetospheric contamination, the map of relative uncertainties estimated from the apogee data set was used (Figure 2 shows the example for energy step 6). All errors except the statistical error are systematic and do not become smaller if the signal is averaged over several pixels.

Figure 5 shows the five different error sources and the resulting total uncertainty (black bars) for energy steps 1, 3, 5, and 7. All values are given as a dimensionless ratio of uncertainty over signal. They were calculated from the median over those ram pixels in the average maps, for which the total uncertainty was smaller than the signal. The striped bars represent the observed temporal variability of the signal, i.e., the standard deviation of the signal over the five years of observation. For ram observations, the observed temporal variability is obviously a good proxy for the total uncertainty estimated from error analysis. The errors increase from typically 30% at solar wind energies to typically 60% at the lowest energy bin at 0.01 keV. This confirms Fuselier et al. (2014) who used error bars of 30% for energy steps 5–8 and 50% for steps 1–4. For antiram observations, the average error exceeds the signal below energy step 6, and the true uncertainty is notably larger than the temporal variability since the latter does not reveal all systematic errors. For ram observations, our analysis illustrates that the statistical error (red bars) and magnetospheric contamination

(green bars) are the two dominating error sources at all energies. The accuracy of IBEX-Lo maps and spectra, therefore, can most efficiently be improved if additional years of observation become available or if a data set with less magnetospheric contamination can be generated.

The total errors illustrated in Figure 5 will serve as the 1σ uncertainty for the map pixels in the following Section 3.1. For energy spectra (Section 3.2), the uncertainty of the absolute instrument calibration ($\sim 30\%$, Fuselier et al. 2009) should also be included. Since this error does not vary with time, it is not relevant for spatial patterns at a given energy, i.e., for interpreting maps. It is relevant for spectra, but at the same time the statistical uncertainty decreases to a negligible amount because an entry in the energy spectrum is an average over typically 12 neighboring map pixels. The two effects cancel each other out because the statistical uncertainty of a single pixel after five years of observations is also 30%. Thus, the average uncertainty of the map pixels will serve as the uncertainty of the energy spectrum value. For the annual changes of the ENA signal (Section 3.3), the standard deviation over the pixel-by-pixel differences will serve as error estimate.

3. RESULTS

In the previous section, we explained how we derived maps of corrected ENA intensity from raw count rates. Here, we first present a sequence of maps to illustrate the various steps of the procedure: Figure 6 shows the maps of raw ENA intensities in the spacecraft reference frame, including the LISM signal and the local background. In Figure 7, these two background sources were suppressed, but the ENA intensities are still in the spacecraft reference frame. Figures 8 and 9 then present all-sky maps and ram-only maps of the final corrected ENA intensity in the solar inertial frame. The left column of the maps shows the ENA intensities (raw or corrected) averaged over all 10 seasons. The right column shows the standard deviation of the signal in case of raw intensities or the relative uncertainty in the case of corrected intensities. The uncertainty estimate takes into account the background sources (magnetospheric contamination, background level), the uncertainty introduced by converting raw counts into corrected intensity (survival probabilities, throughput correction of instrument) and the statistical uncertainty. All maps in this paper are centered on the ecliptic coordinates ($\lambda = 259^\circ$, $\beta = 0^\circ$).

Figure 6 presents the raw ENA intensities measured in energy steps 4–8 for energies 0.11–1.821 keV. The left column shows the average intensity in $\text{cm}^{-2} \text{sr}^{-1} \text{s}^{-1} \text{keV}^{-1}$, the right column shows the ratio of standard deviation to signal. Map pixels with a ratio larger than one were omitted. The absolute intensity differs for each energy step. At solar wind energies (energy steps 7 and 8), the ribbon and the hole around $\lambda = 15^\circ$ are clearly visible even before correcting the intensities for reionization losses and the Compton–Getting effect. In the top panel at 0.11 keV, the signal of sputtered hydrogen from LISM helium overwhelms all other signals (also see Figure 3).

The next series of maps in Figure 7 illustrates an intermediate step of the correction algorithm. The LISM contaminated pixels in the lower energy bins have been suppressed and the ubiquitous background has been subtracted. The plot format is identical to the previous Figure 6, pixels with a temporal variability larger than the signal are blanked out as well. The maps of the two energy steps 7 and 8 above 0.5 keV are identical to the previous figure, whereas the color scales for energy steps 4–6 have been adjusted. The final step of signal reconstruction is

reached with Figure 8, for which the transformation described in Section 2.2 has been applied to the clean maps in Figure 7. The left column in Figure 8 shows the corrected ENA intensities at 100 AU distance to the Sun in the inertial reference frame. The right column shows the total uncertainty due to statistics and systematic errors. This uncertainty is again indicated as a dimensionless ratio of uncertainty to signal. Now all pixels are shown, including those with an uncertainty much larger than the signal. The dashed lines indicate the region where only ram observations exist, the areas outside the solid lines were only covered with antiram observations. These maps demonstrate that antiram pixels at lower energies are severely affected by magnetospheric contamination and poor signal-to-noise ratio. The ENA intensities derived for that hemisphere currently cannot be used to constrain the heliospheric signal. In contrast, the error maps for energy steps 7 and 8 indicate that only the two regions at $\lambda = 130^\circ \dots 170^\circ$ and $\lambda = 0^\circ \dots 30^\circ$ should not be trusted. This uncertainty is caused by magnetospheric contamination. The rectangles in the bottom panel of Figure 8 outline the regions for which we sampled energy spectra (see Section 3.2).

Because of the large uncertainty inherent to antiram observations, we decided to rely on ram-only maps at low energies. Figure 9 presents the cleanest possible maps of the reconstructed heliosphere ENA signal at a 100 AU distance from 0.1 to 1.8 keV. Map pixels covered only in one single season or with a total uncertainty larger than the signal were excluded. The obvious shortcoming of these maps is the gap from 0° to 140° longitude because IBEX is inside the Earth’s magnetosphere most of the time between July and October. This is, in particular, a problem for studying the downwind region of low ENA intensities, which is only marginally covered by the ram observations. For ram observations, some regions in the sky exist for which the uncertainties are smaller than the signal even for energies below 0.1 keV. Figure 10 shows the corrected ENA intensities and the errors for energy steps 1 (0.015 keV) to 3 (0.055 keV) in the same format as Figure 9. Since we excised the LISM signal assuming an energy-dependent threshold for LISM contamination (see Section 2.3), the white area grows as we proceed to the lowest energy. Figure 11 is a different version of Figure 10 with a more stringent LISM contamination threshold (see Section 2.3) as the only difference. All pixels with an intensity exceeding the average intensity plus one standard deviation (1σ) instead of 3σ were excluded. In the following, we will first interpret the maps of corrected intensities (Section 3.1) before we derive energy spectra for selected regions in the maps (Section 3.2). The discussion of the temporal evolution of the energy spectra (Section 3.3) will conclude the results section.

3.1. The Heliospheric Ribbon and the Downwind Direction at Low Energies

To quantify the shape and strength of the ENA ribbon and the ENA hole, we converted the ram maps (Figures 9 and 10) into contour maps using the same color scheme for all energies. The result is shown in Figure 12 for all eight energies. The yellow contours include all intensities significantly above average ($j > \mu + 1\sigma$), whereas red, for instance, indicates $j > \mu + 3\sigma$. The black curves outline the ribbon as it is observed in IBEX-Hi (McComas et al. 2012). The rings are centered at $(\lambda, \beta) = (221^\circ, 39^\circ)$ (Schwadron et al. 2011) and are approximately 40° apart.

From 1.8 keV to 0.4 keV (energy steps 6–8), the shape of the ENA ribbon does not change notably. If we interpret the yellow

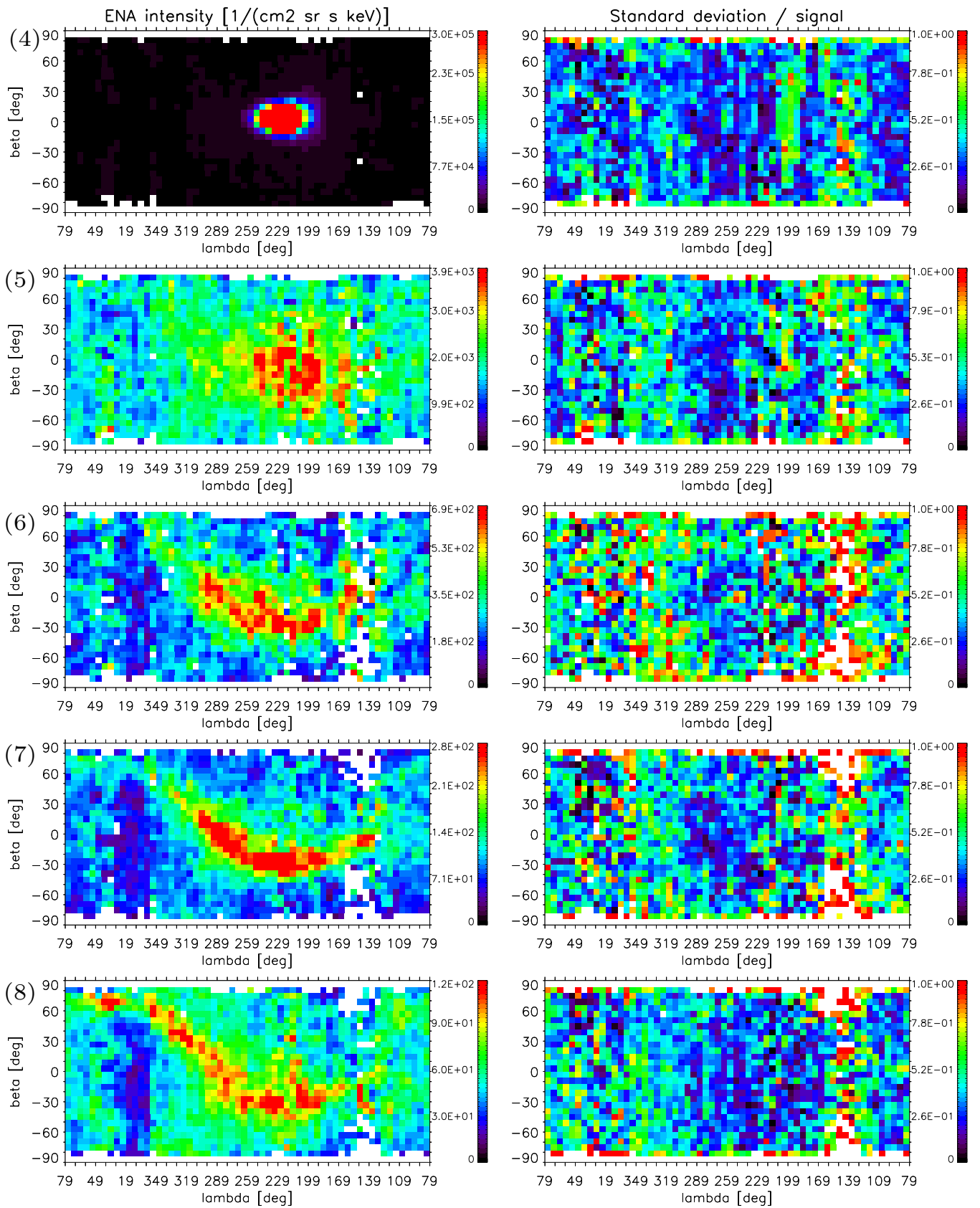


Figure 6. Left column: maps of raw intensity in $\text{cm}^{-2} \text{sr}^{-1} \text{s}^{-1} \text{keV}^{-1}$ for the five energy bins 4 (0.11 keV), 5 (0.209 keV), 6 (0.439 keV), 7 (0.872 keV), and 8 (1.821 keV), averaged over five years. Right column: relative temporal variability over five years. Pixels with a variability larger than the average signal were omitted. (A color version of this figure is available in the online journal.)

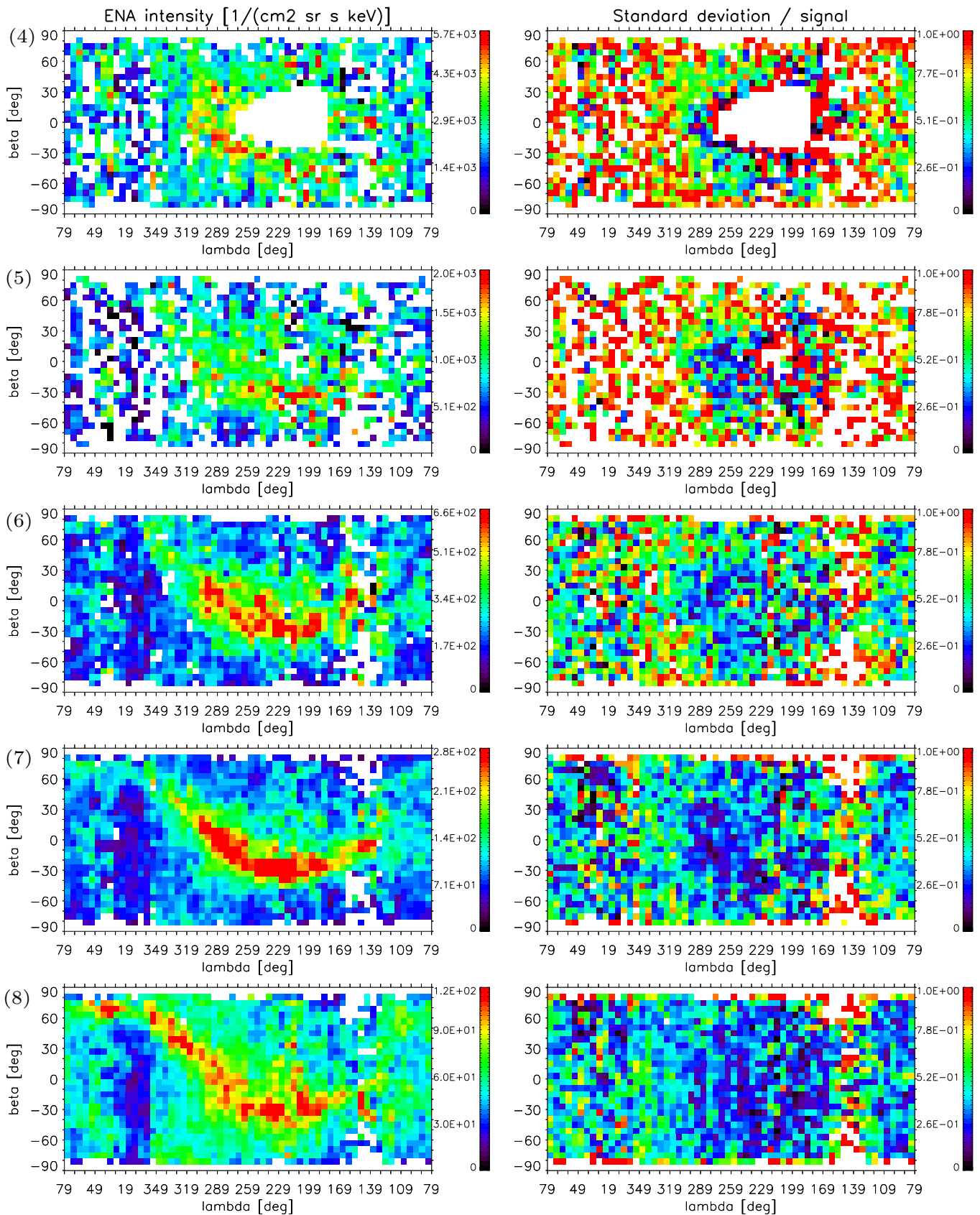


Figure 7. Maps of average ENA intensity in $\text{cm}^{-2} \text{sr}^{-1} \text{s}^{-1} \text{keV}^{-1}$ (left column) and its relative standard deviation (right column) for the five upper energy bins of IBEX-Lo (4, 5, 6, 7, and 8), after subtracting the ubiquitous background and blanking out LISM contaminated pixels. Same format as Figure 6.

(A color version of this figure is available in the online journal.)

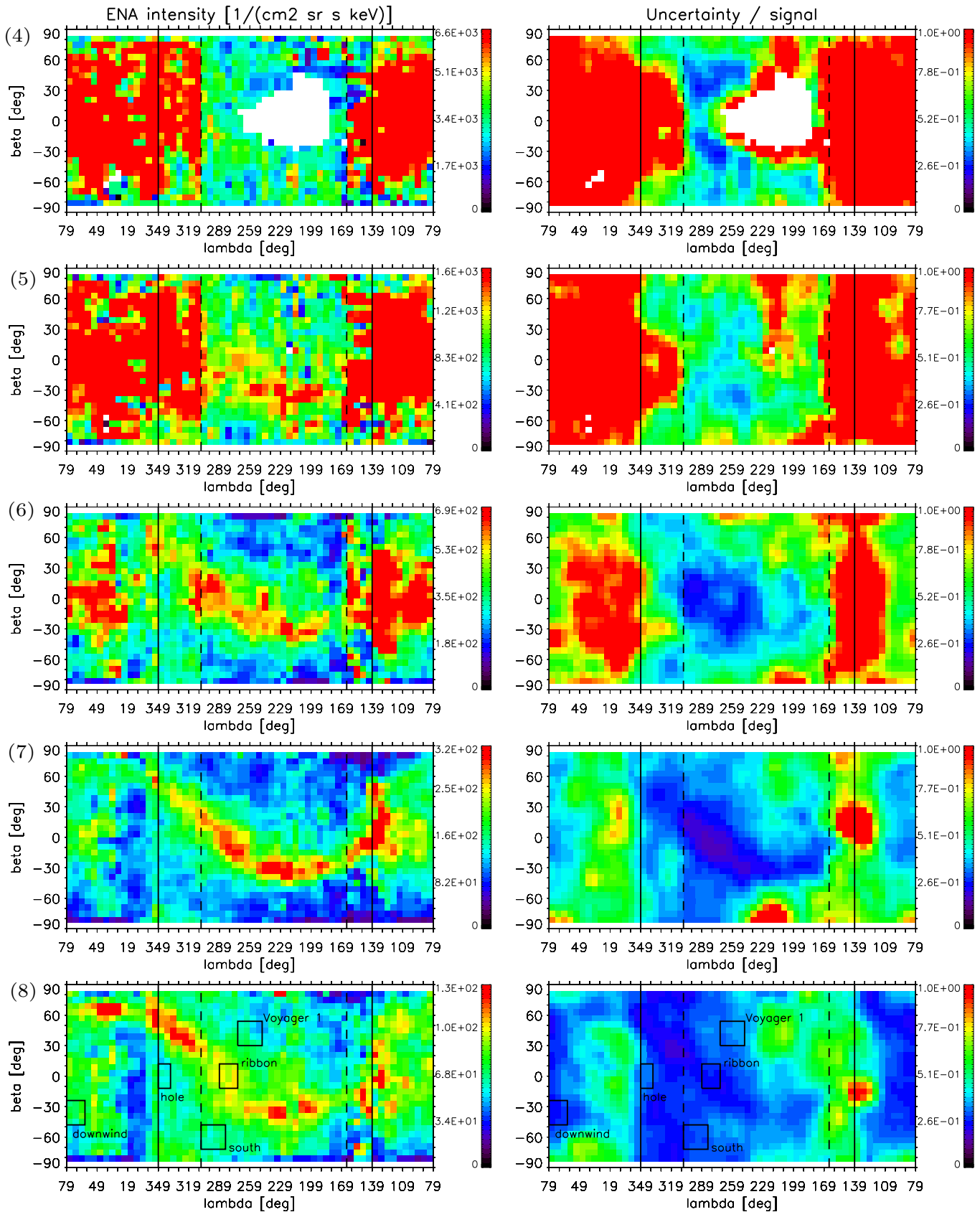


Figure 8. Left column: maps of average heliospheric ENA intensity in $\text{cm}^{-2} \text{sr}^{-1} \text{s}^{-1} \text{keV}^{-1}$ corrected for survival probabilities and Compton–Getting. Right column: relative 1σ uncertainties of the signal (error sources shown in Figure 5). Within the dashed lines, only ram observations are available; outside the solid lines, only antiram observations. The rectangles in the bottom panel outline the regions where we sampled energy spectra.

(A color version of this figure is available in the online journal.)

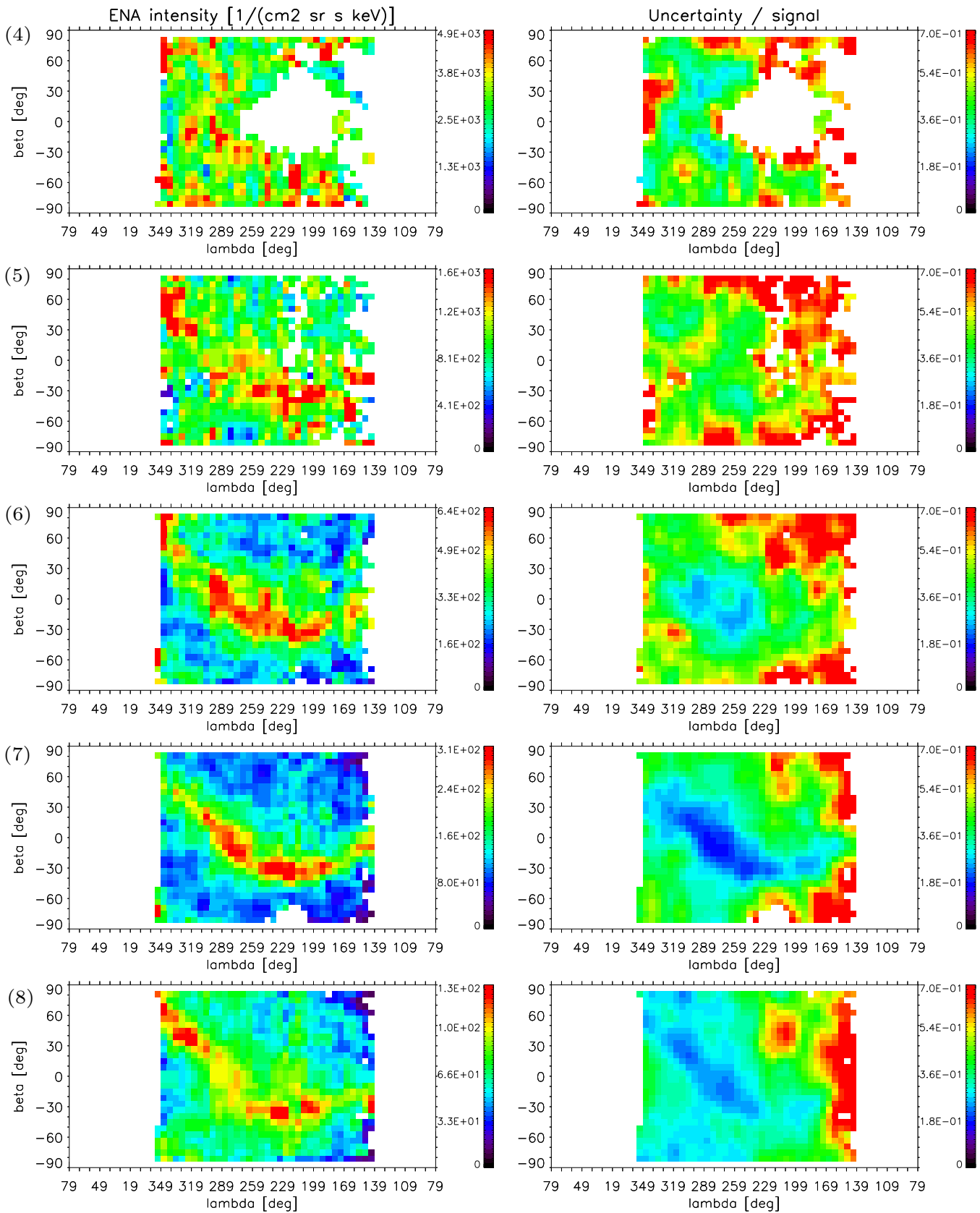


Figure 9. Heliospheric ENA signal corrected for survival probabilities and Compton–Getting; same format as Figure 8 but for measurements in ram direction only. The sector between 0° and 150° longitude is missing because *IBEX* was inside the terrestrial magnetosphere from June until October (see Figure 1). Pixels covered only in a single season or with an uncertainty larger than the signal are not shown. (A color version of this figure is available in the online journal.)

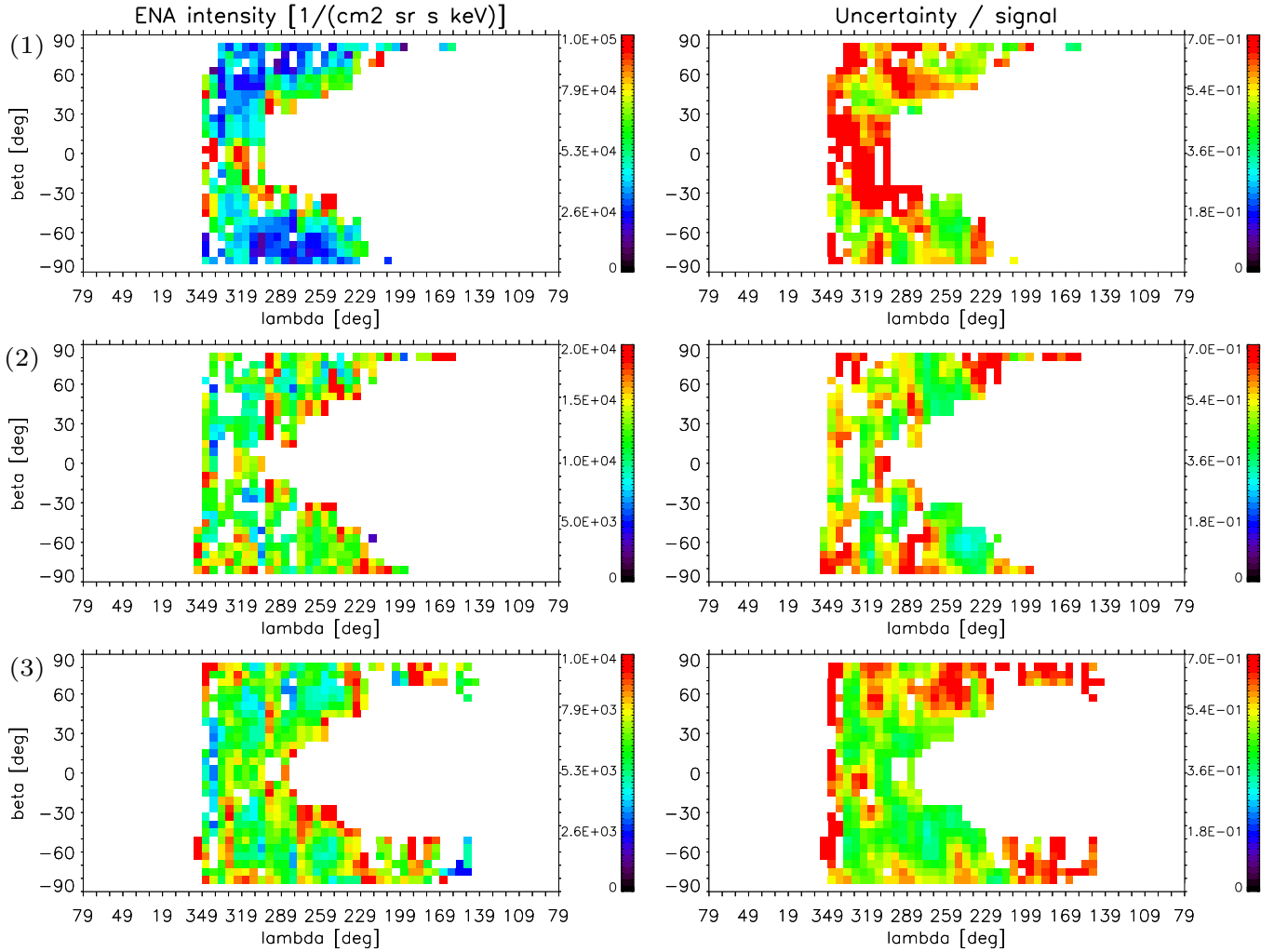


Figure 10. Corrected maps (background, LISM, survival probability, Compton–Getting) for the three lowest energy steps 1 (0.015 keV), 2 (0.029 keV), and 3 (0.055 keV) for measurements in the ram direction, same format as Figure 9. The region of the suppressed LISM inflow shows up as a white wedge. (A color version of this figure is available in the online journal.)

contour line in Figure 12 as the separator between the ribbon and the globally distributed flux (GDF), the average width of the ribbon over the entire hemisphere is $30^\circ \pm 10^\circ$. The full width half maximum of the ribbon at its broadest point (nose) increases from 30° to 50° from solar wind energies down to 0.2 keV (Schwadron et al. 2014). At 0.2 keV (step 5), the ribbon starts to disintegrate. The continuous area of significantly higher intensities breaks apart at 300° longitude, but isolated areas inside the nominal ribbon boundaries close to the ecliptic and at 60° north persist. For IBEX-Hi measurements above 1 keV, McComas et al. (2012) noted that the position of dominant emission in the ribbon changes with energy. The IBEX-Lo maps confirm that the dominant emissions shift from ecliptic poles (energy step 8) to the ecliptic plane (energy step 7) as the ENA energy decreases from several keV to slow solar wind at 1 keV. This observation was interpreted as evidence for a solar wind origin of the ENA ribbon. For lower energies, Figure 12 does not show a uniform trend for maximum ribbon intensities to be pushed closer to the ecliptic plane. To the north, an isolated spot of high ENA intensities persists to 0.1 keV. The ratio of ribbon intensity versus GDF (pixels inside versus outside black curves in Figure 12) evaluate to 1.4 (1.8 keV), 1.7 (0.9 keV), 1.6 (0.4 keV), 1.3 (0.2 keV), and 1.0 (0.1 keV).

This sequence confirms the visual impression that the ribbon is most pronounced between 0.5 and 1 keV and then starts to fade at 0.2 keV. The intensity ratio of the ribbon and the GDF peaks at solar wind energy. This argues for a solar-wind-related production process of the ribbon (Kucharek et al. 2013; Heerikhuisen et al. 2010). Members of the *IBEX* science team (Schwadron et al. 2014) are currently working on a more detailed analysis of the ribbon with respect to the GDF below and above solar wind energies as a follow-up study to Schwadron et al. (2011).

The energy bin at 0.1 keV (step 4) represents the lowest energy where a signature of the ribbon can be observed. There is no longer a continuous region of high intensities inside the expected ribbon region, but remnant spots of high ENA intensities can still be observed to the south and to the Port direction with respect to the LISM inflow region, whereas no intensity enhancements appear to the north. For the three lowest energy steps (0.02–0.06 keV), this north–south dichotomy no longer exists. The only persistent pattern in Figure 12 at energies below 0.1 keV is the halo around the blanked out LISM region centered at $(\lambda, \beta) = (225^\circ, 3^\circ)$. This signal very likely originates from a hot population of neutral helium (Kubiak et al. 2014) and hydrogen LISM atoms too tenuous to be rejected by the cleaning algorithm.

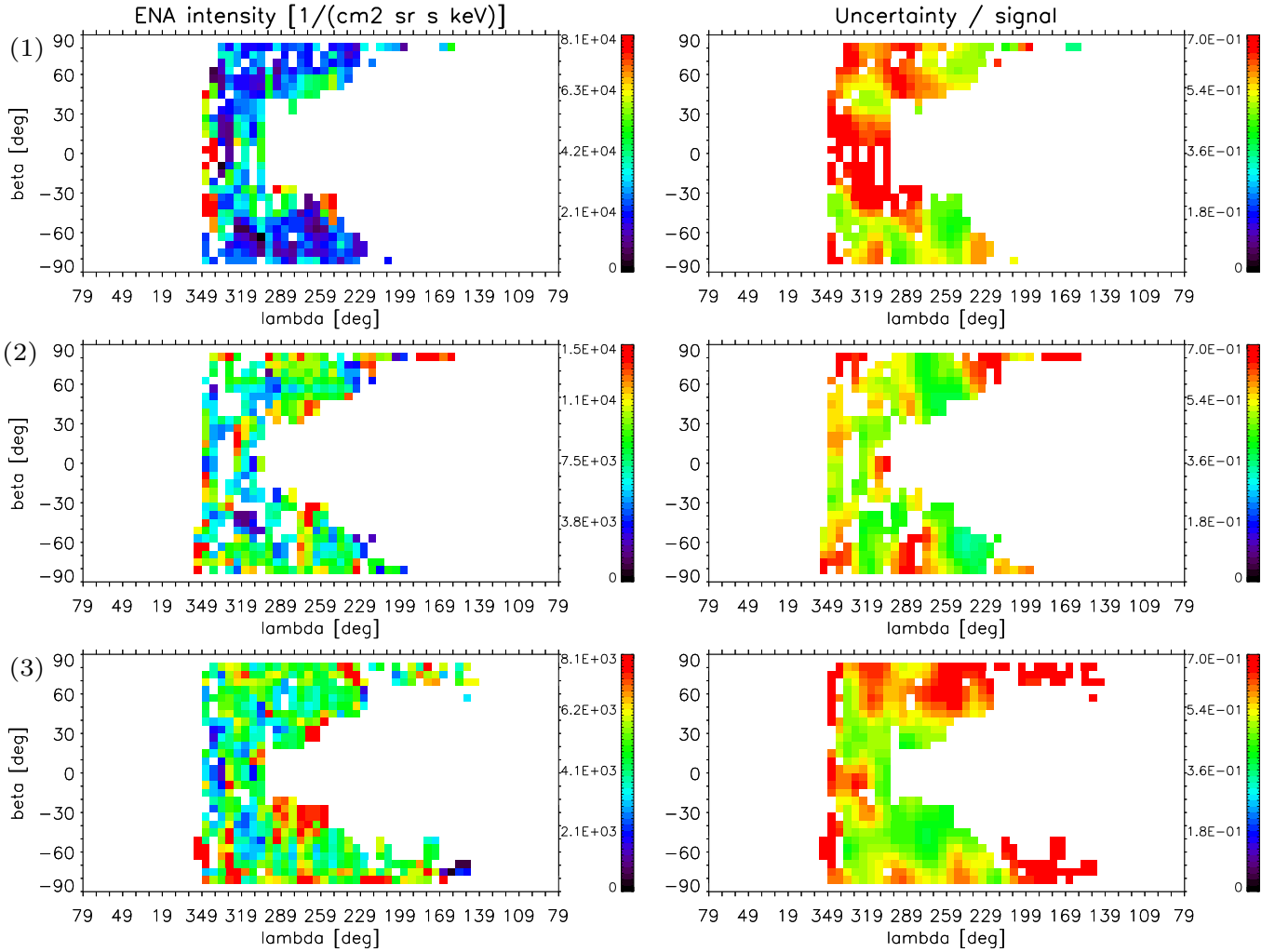


Figure 11. Corrected maps (background, LISM, survival probability, Compton–Getting) for the three lowest energy steps 1 (0.015 keV), 2 (0.029 keV), and 3 (0.055 keV) for measurements in the ram direction. Compared to Figure 10, the threshold that excludes LISM contaminated pixels was lowered from $\mu + 3\sigma$ to $\mu + 1\sigma$ of the raw count rates outside the LISM region. As a result, the white areas become larger.

(A color version of this figure is available in the online journal.)

We therefore created maps (Figure 11) for the three lowest energy steps assuming a more stringent threshold value for LISM contamination: we use one standard deviation of the uncontaminated raw count rates instead of the default three standard deviations. The white areas grow and the halo around the LISM region in energy steps 2 and 3 vanishes. The remaining heliospheric signal shows no spatial patterns. Its average intensity is 15% to 20% lower compared to the previous Figure 10 because the more stringent LISM threshold also rejected the most intense pixels outside the expected LISM inflow region. If this effect is taken into account, the energy spectra (see Section 3.2) derived from Figures 10 and 11 agree with each other. The energy spectrum entries obtained at regions that are only covered with the less stringent LISM contamination threshold will be interpreted as upper limits on heliospheric ENAs. For the lowest energy step, a bright rim around the LISM region persists also in Figure 11. It seems that, for this energy (0.015 keV), the LISM inflow is too extended to derive a full map of heliospheric ENAs with our current knowledge. Only close to the poles do we see two small regions where we can estimate the intensity of the GDF without LISM contribution.

We conclude that the ENA ribbon starts to fragment at 0.2 keV while some remnant spots of increased intensity can

be identified down to 0.1 keV. At lower energies, we do not observe any heliospheric ribbon-like pattern between 280° and 360° ecliptic longitude, independent of the chosen threshold for LISM contamination.

Adjacent to the ENA ribbon, two regions of low ENA intensities appear at solar wind energies in the complete ENA maps (see the bluish regions in the two lower panels of Figure 8). A circular hole exists toward the heliospheric nose direction, centered at (221°, 39°), and an oval region extends over the ecliptic and the southern hemisphere at 20° longitude. The latter is close to the downwind direction, but the center of the region is offset from the downwind direction at the map boundary ($\lambda = 79^\circ, \beta = -5^\circ$). The minimum ENA intensity in Figure 8 is found at $15^\circ \pm 5^\circ$ (1.8 keV and 0.9 keV) and $10^\circ \pm 10^\circ$ at (0.4 keV). The position at 1.8 keV agrees with McComas et al. (2013) who observed in IBEX-Hi data that the center of the hole shifts from 33° to 9° as energies decrease from 4.3 to 1.7 keV. No similar energy-dependent shift appears for energies below 1 keV. We remind the reader, however, that any analysis of the downwind region at low energies is severely affected by the magnetospheric background. The latter spreads out from downwind direction to 140° longitude at lower energies and thus could introduce a spurious shift of the

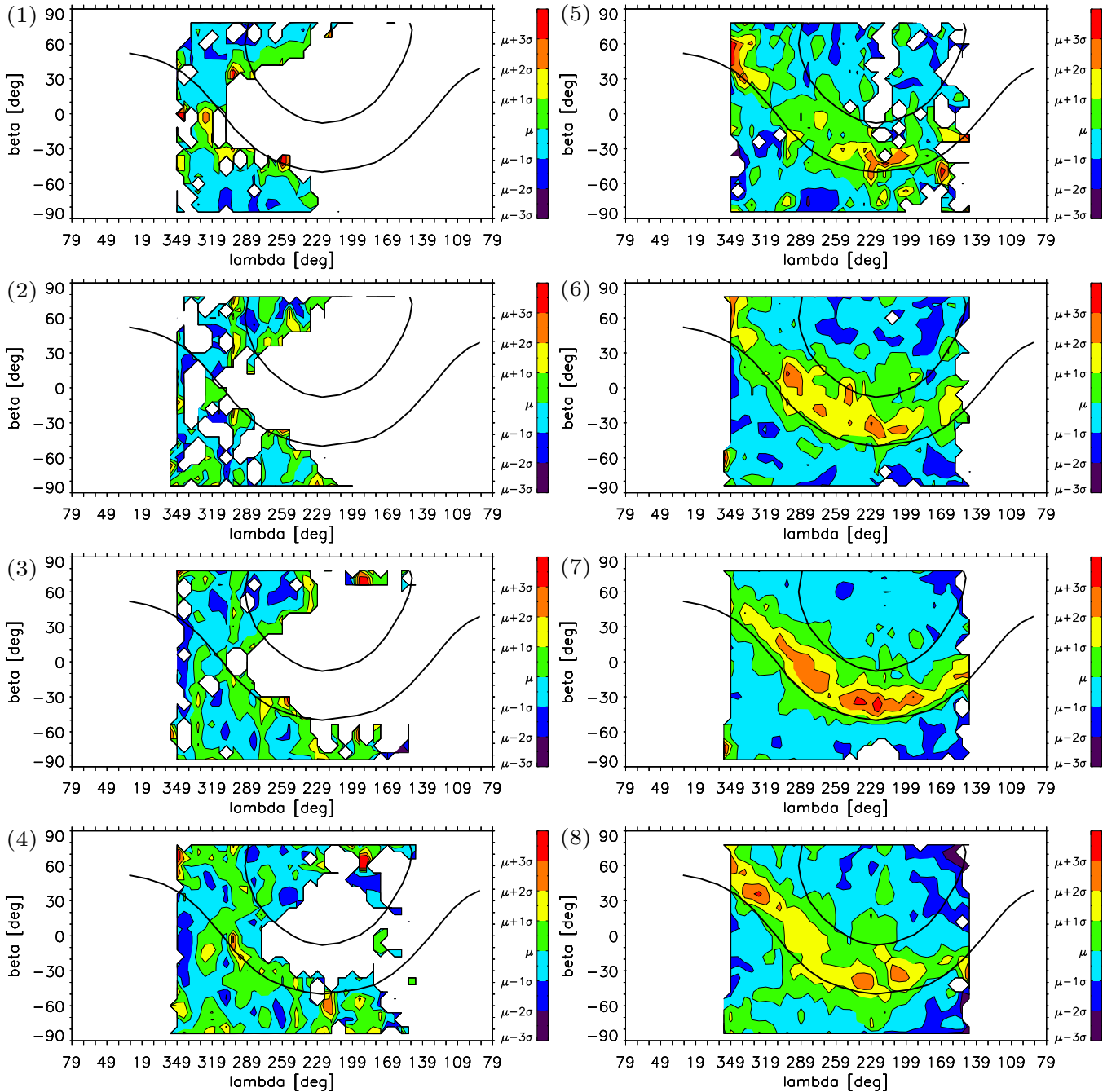


Figure 12. Contour plot of the ram maps of corrected ENA intensities (see Figures 9 and 10) for all eight energy bins. The position of the ENA ribbon as parameterized by McComas et al. (2012) is indicated by the black lines.

(A color version of this figure is available in the online journal.)

heliospheric ENA signal with energy. Given the uncertainties of antiram observations (see right column of Figure 8), we cannot confidently identify the center of the hole for energies below 0.5 keV. If we rely on uncorrected antiram maps to reduce the impact of magnetospheric contamination, we find that the center of the hole appears at $20^\circ \pm 10^\circ$ ecliptic longitude for all eight energy bins. The present study allows us to make a confident statement only about the rim of the hole at 335° longitude. This position does not change with energy either, we can follow its trace in Figure 12 from 1.8 keV down to 0.055 keV. In the two lowest energy bins, virtually all relevant pixels are affected by large uncertainties (see Figure 10).

Schwadron et al. (2011) considered the possibility that the hole in ENA intensities observed at solar wind energies at $\sim 44^\circ$ west (see, e.g., Figure 8) of the interstellar downwind direction corresponds to the tail direction of the heliosphere. Taking the center of the ribbon ($221^\circ, 39^\circ$) as the direction of the LISM magnetic field, they noted that the ENA hole is approximately between the interstellar downwind direction and the direction along the interstellar magnetic field. However, the interpretation of the region of low ENA intensities as the heliotail direction faces a problem. $\text{Ly}\alpha$ absorption lines toward nearby stars in the downwind direction show that the heliotail must be aligned with the LISM downwind direction within 20° as we

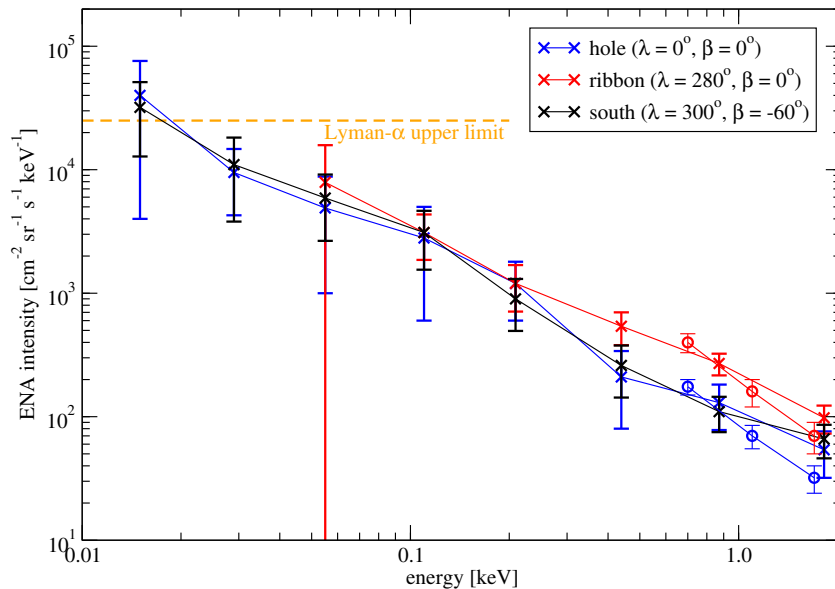


Figure 13. ENA energy spectra for three different regions for which ram measurements are available. Blue: boundary of the low ENA intensity region, red: ribbon pixels in the ecliptic, black: region in the southern hemisphere. The orange dashed line indicates the upper limit on heliospheric ENAs derived from Ly α observations, circles indicate observations obtained with IBEX-Hi for the overlapping energy range. Error bars of IBEX-Hi represent the spatial variability within averaging box. (A color version of this figure is available in the online journal.)

approach the energies of thermal hydrogen (Wood et al. 2007). For the energies where the ribbon is completely gone, i.e., below 0.1 keV, the ENA emissions from the heliotail region should thus be organized around the nominal downwind direction. We unfortunately cannot verify this prediction because of the insufficient signal-to-noise ratio for antiram observations. We cannot verify either if the heliotail continues to be a low intensity region for energies below 0.5 keV or if it becomes a source region of ENAs, as predicted by some models (Zank et al. 2010; Gruntman et al. 2001).

3.2. Energy Spectra of Heliospheric ENAs

We compiled energy spectra from the five regions in the ENA intensity maps depicted in the bottom panel of Figure 8: *Voyager 1* direction ($\lambda = 258^\circ$, $\beta = 36^\circ$), LISM downwind direction (70° , -36°), southern hemisphere (300° , -60°), ribbon (280° , 0°), and the rim of the ENA hole at (350° , 0°). The first two directions are identical to the choices by Fuselier et al. (2014) to allow for a comparison, the ribbon and the hole represent regions of very high and very low ENA intensities. At (300° , -60°), we have the smallest uncertainties at very low energies. Except for the downwind direction, all spectra were derived from the pixels in ram maps with a relative uncertainty smaller than one (see Figures 9 and 10). The spectral entries were derived as average over 3×4 or 4×4 pixels, the error bar is the average of the pixels shown in the right column of the intensity maps. If a region at a given energy is only covered with the less stringent LISM contamination threshold, the derived value is interpreted as an upper limit of heliospheric ENA intensity and the relative uncertainty is set to unity (for instance, the *Voyager 1* spectrum in energy steps 1 and 2).

Figures 13 (ribbon pixel, southern hemisphere, and rim of hole) and 14 (*Voyager 1* direction) show energy spectra for the entire energy range covered by IBEX-Lo (1.8 to 0.015 keV). In the second figure, we compare our results to Fuselier et al. (2014) for the same region. Compared to the present study, Fuselier et al. (2014) did not subtract the local background, and they

used a different approach to correct for the Compton–Getting effect. They applied 30% relative error bars to energy steps 5–8 and 50% relative error bars to energy steps 1–4 unless the statistical uncertainty exceeded these values. The values below 0.1 keV (shown here as gray circles) were interpreted by Fuselier et al. (2014) as upper limits of the true heliospheric signal. The orange dashed lines indicate the upper limits on low energy hydrogen atoms between 0.01 and 0.2 keV derived from Ly α observations of nearby stars (Wood et al. 2007). Fuselier et al. (2014) assumed an upper limit of $10^5 \text{ cm}^{-2} \text{ sr}^{-1} \text{ s}^{-1} \text{ keV}^{-1}$ for *Voyager 1* direction and $5 \times 10^3 \text{ cm}^{-2} \text{ sr}^{-1} \text{ s}^{-1} \text{ keV}^{-1}$ for downwind direction. We assumed an intermediate value of $2.5 \times 10^4 \text{ cm}^{-2} \text{ sr}^{-1} \text{ s}^{-1} \text{ keV}^{-1}$ for the other directions. For the downwind direction, the error bars of the spectrum are larger than the signal for all energies below 0.5 keV. This is unfortunate, since Ly α observations would place a more stringent upper limit on the heliospheric ENAs from that region. ENA intensities measured with IBEX-Hi at 0.7, 1.1, and 1.7 keV (Figure 14 in McComas et al. 2012), are shown as circles in Figures 13 and 14, the error bars represent spatial variability. Table 2 summarizes the energy spectra for all five regions in the sky including the downwind direction and the rim of the hole, which are not shown in Figures 13 and 14.

Due to the subtraction of the background, the energy spectra of the heliospheric ENA signal are consistent with the upper limits derived from Ly α observations for all-sky directions (see Figures 13 and 14). The energy spectrum of heliospheric ENAs looks uniform at energies below 0.2 keV for different regions. Above 0.2 keV, the ENA ribbon becomes statistically significant also in this spectral plot (compare the blue and the red lines in Figure 13). IBEX-Hi observations imply a steeper power law than IBEX-Lo for the overlapping energy range at 0.5 to 2.0 keV, but the absolute intensities agree with each other. A knee in the energy spectrum of heliospheric ENAs around 1 keV was also observed earlier with the ASPERA-3/4 experiments on board Mars Express and Venus Express (Galli et al. 2013). As for the spectral slope at lower energies, the ENA intensities observed with IBEX-Lo seem to follow

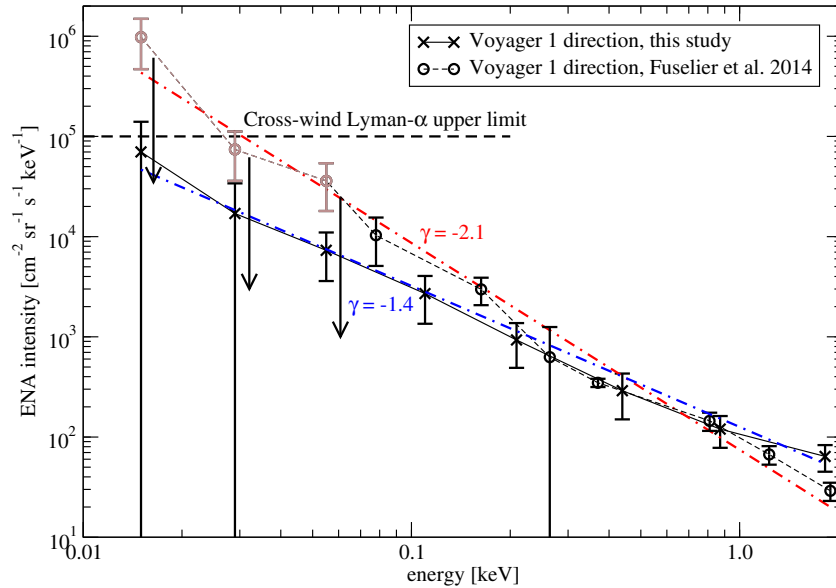


Figure 14. Energy spectra for *Voyager 1* direction: “x,” this study; circles, Fuselier et al. (2014) (arrows indicate that the value is to be understood as the upper limit). The difference at lower energies is introduced by the subtraction of local background in the present study. The horizontal dashed line indicates the upper limit on heliospheric ENAs derived from Ly α observations, dash-dotted lines illustrate power-law fits to the two spectra.

(A color version of this figure is available in the online journal.)

Table 2
Corrected Energy Spectra of Heliospheric ENA Intensities in Units of $\text{cm}^{-2} \text{sr}^{-1} \text{s}^{-1} \text{keV}^{-1}$, Averaged over All Observations from 2009 to 2013 from Five Different Regions in the Sky (Outlined in the Bottom Panel of Figure 8)

Energy	<i>Voyager 1</i>	Ribbon	South	Hole	Downwind
0.015 keV	70000 ± 70000	N/A	32000 ± 19200	40000 ± 36000	380000 ± 950000
0.029 keV	17000 ± 17000	N7/A	11000 ± 7200	9500 ± 5225	73000 ± 150000
0.055 keV	7300 ± 3700	7900 ± 7900	5900 ± 3245	4900 ± 3900	15000 ± 30000
0.110 keV	2700 ± 1350	3100 ± 1240	3100 ± 1550	2800 ± 2200	9100 ± 18000
0.209 keV	930 ± 440	1200 ± 490	900 ± 405	1200 ± 600	1600 ± 1600
0.439 keV	290 ± 140	540 ± 160	260 ± 117	210 ± 130	350 ± 280
0.872 keV	120 ± 42	270 ± 54	110 ± 35	130 ± 52	130 ± 46
1.821 keV	64 ± 19	98 ± 25	66 ± 20	54 ± 22	73 ± 22

Note. *Voyager 1*: ($\lambda = 258^\circ$, $\beta = 36^\circ$); ribbon: ($\lambda = 280^\circ$, $\beta = 0^\circ$); south: ($\lambda = 300^\circ$, $\beta = -60^\circ$); hole: ($\lambda = 350^\circ$, $\beta = 0^\circ$); and downwind: ($\lambda = 70^\circ$, $\beta = -36^\circ$). Except for downwind direction, only ram pixels with a relative uncertainty less than one were used for these averages.

a uniform power law with an exponent $\gamma = -2.1 \pm 0.1$ if the ubiquitous background is not subtracted. The background subtraction introduced in the present analysis results in a flatter spectrum with $\gamma = -1.4 \pm 0.1$ if a uniform power law is assumed for the entire IBEX-Lo energy range. For theoretical reasons, we expect the heliospheric ENA spectrum to drop off at lower energies. In Figure 13, the spectral slopes change around 0.1 keV from $\gamma = -1.8$ to -0.9 in the southern hemisphere and at the rim of the ENA hole. This indicates that the rollover of heliospheric ENAs starts at this energy, but the measurement uncertainties do not allow for a definite answer. The uniform power law with $\gamma = -1.4 \pm 0.1$ reproduces the measured intensities within their error bars at all eight energies.

The decrease of ENA intensities with respect to previous work (Fuselier et al. 2014) has some impact on the assumed origin of the ENAs below 0.5 keV. Desai et al. (2014) assumed that a model should predict a heliospheric ENA intensity of $\sim 5000 \text{ cm}^{-2} \text{ sr}^{-1} \text{ s}^{-1} \text{ keV}^{-1}$ at 0.1 keV for *Voyager 1* and *Voyager 2* directions to reproduce IBEX observations. Comparing different models, they concluded that an origin in the outer heliosheath for the ENAs observed below 0.5 keV energy is likely (Zirnstein et al. 2014), since models including only ENA sources in the inner heliosheath (Gloeckler & Fisk 2010; Zank et al.

2010) predict only $\sim 1000 \text{ cm}^{-2} \text{ sr}^{-1} \text{ s}^{-1} \text{ keV}^{-1}$ intensity at this energy. Desai et al. (2014) suggested that “a significant fraction of the low energy ENAs between ~ 0.1 and 0.5 keV observed by IBEX could be created by a nonthermalized hotter, pickup-ion population” in the outer heliosheath. For ENAs above 0.5 keV, on the other hand, also Desai et al. (2014) assumed an origin in the inner heliosheath. The new energy spectra presented here in Figures 13 and 14 indicate an ENA intensity of only $3000 \text{ cm}^{-2} \text{ sr}^{-1} \text{ s}^{-1} \text{ keV}^{-1}$ at 0.1 keV. These results still exceed the predictions by Gloeckler & Fisk (2010) and Zank et al. (2010), but they call for a smaller contribution from hot pickup ions in the outer heliosheath.

3.3. Temporal Variability

If a region in the heliospheric ENA intensity maps can be observed to evolve with time, the timescale will tell us something about the distance at which the ENAs were generated. Fast variations of the ribbon structure, e.g., would point to a rather close ENA production near the termination shock (McComas et al. 2014b). In contrast, the intensity of the GDF at 0.2 keV should not vary over a few years if the ENAs originate in the outer heliosheath (Zirnstein et al. 2014). Statistical noise

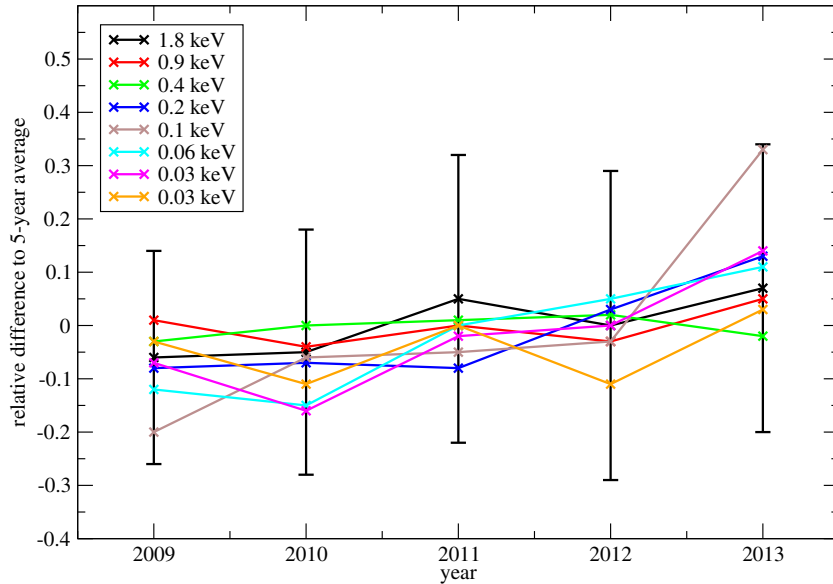


Figure 15. Annual relative changes of heliospheric ENA intensities, averaged over the entire ram maps in Figures 9 and 10. The error bars represent the standard deviations of the pixel-by-pixel differences.

(A color version of this figure is available in the online journal.)

and orbit-to-orbit differences due to magnetospheric variability make studies of the temporal evolution of heliospheric ENAs at low energies challenging. For the present study, we restricted ourselves to a comparison of the annual ENA intensity averaged over the whole ram hemisphere.

Figure 15 shows the relative annual change of ENA intensities. For each pixel in the ram maps (Figures 9 and 10), we calculated the relative difference between a single year and the five-year average. The mean over all pixels is the estimate for the annual change, the error bars indicate the standard deviations. They range from 25% to 40% for all energies and years. Considering the error bars, we do not observe any significant change of the heliospheric signal with time. IBEX-Hi observations also indicate that the relative change of ENA intensities from 2009 to 2013 is less than 20% for all regions at 0.7 keV (McComas et al. 2014a). On the other hand, IBEX-Lo 8 (1.8 keV) currently does not confirm the decrease of heliospheric ENA intensities above 1 keV observed with IBEX-Hi between 2009 and 2012. The current IBEX-Lo analysis only proves that the heliospheric ENA signal observed in ram direction between 2 keV and 0.015 keV did not vary by more than 30% from 2009 to 2013. The same conclusion is reached from error analysis (see Section 2.4): the observed temporal variability over five years is not notably larger than the total uncertainty at any energy. Since the total uncertainty does not include any term for heliospheric variability, the latter must be smaller than the 30% of the dominant error sources (statistical uncertainty and magnetospheric contamination).

4. CONCLUSIONS

IBEX-Lo measurements have allowed us to extend the range of heliospheric ENA observations to very low energies at 15 eV. The combination of a relatively weak signal and three strong background sources presents a serious challenge to heliospheric ENA imaging in Earth orbit at low energies. Nevertheless, we can confirm the presence of the ENA ribbon and two regions of very low ENA intensities at the *Voyager 1* direction and in the ecliptic plane around $\lambda = 20^\circ$ down to 0.1 keV.

At lower energies, no spatial structure apart from the halo around the LISM inflow direction can be identified in the heliospheric intensities. Future studies on heliospheric ENAs from that direction require a better understanding of the neutral helium and hydrogen populations in the heliosphere. The heliospheric ENA intensities outside the LISM region reach a few $10^4 \text{ cm}^{-2} \text{ sr}^{-1} \text{ s}^{-1} \text{ keV}^{-1}$ below 0.05 keV. The energy spectrum follows a power law with a slope of -1.4 from solar wind energies down to 0.1 keV, where the spectrum probably starts to roll over. The heliospheric ENA signal remains constant within 30% between 2009 and 2013. Additional years of observation and a data subset with less magnetospheric contamination will be most efficient to reduce the uncertainties for the following heliospheric studies with IBEX-Lo. For future missions dedicated to map the heliospheric ENA signal at energies below 0.5 keV, a satellite orbit far away from the Earth’s magnetosphere is strongly recommended.

We thank all of the outstanding men and women who have made the *IBEX* mission such a wonderful success. M.B., M.A.K., and J.M.S. were supported by Polish National Science Center grant 2012-06-M-ST9-00455.

APPENDIX

This appendix specifies, step by step, from raw count rates to frame transformed ENA intensities, the differences between the experimental mapping algorithm employed for this study and the algorithm used for the recently released intensity maps in McComas et al. (2014a).

The mapping algorithm developed for this study relies on histogram data instead of direct event data. Direct event data benefit from a more precise pointing information. On the other hand, a buffer overflow effect may cause strong signals (in particular the LISM inflow) to be underestimated in direct event mode. Given the low count rates of heliospheric ENA signals, a finer spatial resolution than the $6^\circ \times 6^\circ$ offered by histogram data would be useless for the present study, whereas we can avoid the buffer overflow effect that may occur for direct event

data. Both mapping tools rely on triple coincidence hydrogen ENA data.

The *IBEX* team maintain a list of good times for heliospheric ENA observations to minimize background sources. For the present study, we had to exclude the following orbits from that list because they showed an increased background at the lowest energy steps or because they contained only antiram observations: 11–14, 49–51, 169b, 183a, and 184a. We culled the remaining observation times a second time, choosing only those histogram times when the triple counts in 180° of spin angle were ≤ 3 in energy steps 7 and 8. This is the same criterion as used for the maps in previous *IBEX*-Lo publications (Fuselier et al. 2012, 2014; McComas et al. 2014a).

The count rates averaged over the observation time were then corrected for the data throughput limitation caused by electrons (for observations until orbit 168) and the change of post acceleration voltage in summer 2012 (for orbits after 177). These two corrections were not yet included in the *IBEX*-Lo map in McComas et al. (2014a). That study concentrated on the relative changes in efficiency and therefore disregarded the corrections since they partially compensate each other. For the present analysis, the data throughput limitation was corrected by increasing the apparent intensities by the following ratios for energy steps 1–8: 1.08, 1.09, 1.15, 1.33, 1.16, 1.05, 1.04, and 1.04. The data throughput limitation is more pronounced during magnetospheric activity. Thus, the constant ratio is only an approximation, which was taken into account in the error analysis for energy steps 3–5 (see Section 2.4). For future studies, we plan to exclude times with low data throughput ratios because these observations are strongly affected by magnetospheric contamination.

As the next step, we subtracted the sputtering contribution of counts from higher into lower energy bins. We assumed the sputtering ratios derived by Fuselier et al. (2012) (0.06, 0.14, 0.11, 0.12, 0.06, 0.22, 0.18, and 0.14 for energy steps 1–8) to be constant for all viewing directions. For the maps presented by McComas et al. (2014a), the sputtering effect is removed with a more complex bootstrap method from the highest to the lowest energy bin. At very low energies, this method seems to have the drawback that it spreads out small-scale magnetospheric noise from one energy step to the neighboring channels.

After subtracting the background, we transformed the intensity maps from the spacecraft reference frame to the solar reference frame at the center energy of the eight *IBEX*-Lo bins for the entire sky. In the same step, we also corrected for reionization

losses. Fuselier et al. (2014) did a simple frame transformation to derive energy spectra of the heliospheric signal. The *IBEX*-Lo maps presented by McComas et al. (2014a) show ENA intensities in the spacecraft frame, without and with correction for reionization losses. The survival probabilities (Bzowski et al. 2013; Sokół et al. 2013) used to correct for reionization losses are identical for all *IBEX* studies.

REFERENCES

- Bochsler, P., Petersen, L., Möbius, E., et al. 2012, *ApJS*, **198**, 13
- Burlaga, L. F., Ness, N. F., Acuña, M. H., et al. 2008, *Natur*, **454**, 75
- Bzowski, M., Kubiak, M. A., Möbius, E., et al. 2012, *ApJS*, **198**, 12
- Bzowski, M., Sokół, J. M., Tokumaru, M., et al. 2013, in *Cross-Calibration of Past and Present Far UV Spectra of Solar Objects and the Heliosphere*, ISSI Scientific Report Series 13, ed. E. Quémerais, M. Snow, & R. M. Bonnet (New York, NY: Springer), 67
- Desai, M. I., Allegrini, F., Bzowski, M., et al. 2014, *ApJ*, **780**, 98
- Funsten, H. O., Allegrini, F., Bochsler, P., et al. 2009, *SSRv*, **146**, 75
- Fuselier, S. A., Allegrini, F., Bzowski, M., et al. 2012, *ApJ*, **754**, 14
- Fuselier, S. A., Allegrini, F., Bzowski, M., et al. 2014, *ApJ*, **784**, 89
- Fuselier, S. A., Bochsler, P., Chornay, D., et al. 2009, *SSRv*, **146**, 117
- Galli, A., Wurz, P., Kollmann, P., et al. 2013, *ApJ*, **775**, 24
- Gloeckler, G., & Fisk, L. A. 2010, in *AIP Conf. Proc. 1302, Pickup Ions throughout the Heliosphere and Beyond*, ed. J. A. Le Roux, V. Florinski, G. P. Zank, & A. J. Coates (Melville, NY: AIP), 110
- Gruntman, M., Roelof, E. C., Mitchell, et al. 2001, *JGR*, **106**, 15767
- Heerikhuisen, J., Pogorelov, N. V., Zank, G. P., et al. 2010, *ApJL*, **708**, L126
- Kubiak, M. A., Bzowski, M., Sokół, J. M., et al. 2014, *ApJS*, **213**, 29
- Kucharek, H., Fuselier, S. A., Wurz, P., et al. 2013, *ApJ*, **776**, 109
- McComas, D. J., Allegrini, F., Bochsler, P., et al. 2009a, *SSRv*, **146**, 11
- McComas, D. J., Allegrini, F., Bochsler, P., et al. 2009b, *Sci*, **326**, 959
- McComas, D. J., Allegrini, F., Bzowski, M., et al. 2014a, *ApJS*, **213**, 20
- McComas, D. J., Dayeh, M. A., Allegrini, F., et al. 2012, *ApJS*, **203**, 1
- McComas, D. J., Dayeh, M. A., Funsten, H. O., Livadiotis, G., & Schwadron, N. A. 2013, *ApJ*, **771**, 77
- McComas, D. J., Lewis, W. S., & Schwadron, N. A. 2014b, *RvGeo*, **52**, 118
- Möbius, E., Bochsler, P., Bzowski, M., et al. 2012, *ApJS*, **198**, 11
- Richardson, J. D., Kasper, J. C., Wang, et al. 2008, *Natur*, **454**, 63
- Rodriguez Moreno, D. F., Wurz, P., Saul, L., et al. 2013, *A&A*, **557**, A125
- Rodriguez Moreno, D. F., Wurz, P., Saul, L., et al. 2014, *Entrp*, **16**, 1134
- Saul, L., Bzowski, M., Fuselier, S. A., et al. 2013, *ApJ*, **767**, 130
- Schwadron, N. A., Allegrini, F., Bzowski, M., et al. 2011, *ApJ*, **731**, 56
- Schwadron, N. A., Möbius, E., Fuselier, S. A., et al. 2014, *ApJ*, in press
- Schwadron, N. A., Möbius, E., Kucharek, H., et al. 2013, *ApJ*, **775**, 86
- Sokół, J. M., Bzowski, M., Tokumaru, M., Fujiki, K., & McComas, D. J. 2013, *SoPh*, **285**, 167
- Wood, B. E., Izmodenov, V. V., Linsky, J. L., & Malama, Y. G. 2007, *ApJ*, **657**, 609
- Zank, G. P., Heerikhuisen, J., Pogorelov, N. V., Burrows, R., & McComas, D. J. 2010, *ApJ*, **708**, 1092
- Zirnstein, E. J., Heerikhuisen, J., Zank, G. P., et al. 2014, *ApJ*, **783**, 129